optica

Superresolution far-field imaging by coded phase reflectors distributed only along the boundary of synthetic apertures: supplementary material

ANGIKA BULBUL,* A. VIJAYAKUMAR AND JOSEPH ROSEN

Department of Electrical and Computer Engineering, Ben-Gurion University of the Negev, Beer-Sheva P.O. Box 653, 8410501, Israel

**Corresponding author: angikabulbul@gmail.com*

Published 18 December 2018

This document provides supplementary information to "Superresolution far-field imaging by coded phase reflectors distributed only along the boundary of synthetic apertures," https://doi.org/10.1364/OPTICA.5.001607. The supplementary material consists of four sections: The first section describes the generation and design of the aperture function. The second section characterizes the obtained result via Structural Similarity and visibility analysis, and illustrates the superiority of SMART (synthetic marginal aperture with revolving telescopes) and PAIS (partial aperture imaging system) over direct imaging. The third section discusses the SMART and PAIS with a large field of view and the final section describes an experimental demonstration with two spatial light modulators and discusses its results.

1. Design of the Aperture Function

The aperture function library is engineered using a diffractive lens to satisfy the Fourier relation of the Gerchberg-Saxton algorithm (GSA) between the spatial light modulator (SLM) plane and the sensor plane. Additionally, the aperture is designed to deflect the light outside the sub-apertures of the coded phase mask (CPM) away from the sensor. The expression of the diffractive lens is given as $Q(z_h)=\exp\left[-i\pi(z_h\lambda)^{-1}(x^2+y^2)\right]$, where z_h is the distance between the SLM and the sensor plane. To deviate the useless light away from the sensor, a linear phase [1] $L(s_x)=\exp\left[i2\pi\lambda^{-1}(s_x x)\right]$ is combined onto the area outside the sub-apertures. In this case, the design values are λ = 635 *nm*, z_h = 25 *cm* and a linear phase with $s_x \approx$ 0.12. As is shown in Fig. S1, the sub-aperture pair phase profile synthesized by the GSA is multiplied by the phase $Q(z_h)$ and by the linear phase $L(s_x)$, but with zero phase in the regions of the sub-aperture pair. Consequently, the aperture phase function deviates the light which is not incident on the sub-aperture pair away from the sensor. This process is repeated $N(N-1)/2$ times for the entire permutations, where N is the number of points on the synthetic aperture grid. In the present case, N = 8 and hence there are 28 permutations. In total, the process is repeated $3N(N-1)/2$ times to obtain complex holograms.

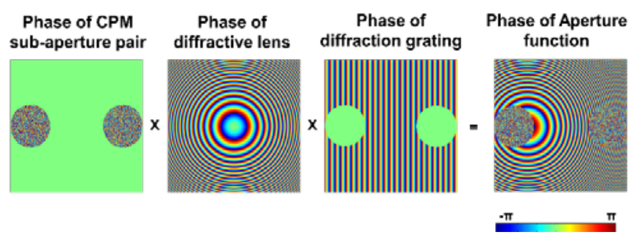

Fig. S1: Design of the aperture function for implementing SMART and PAIS.

2. Structural Similarity and Visibility Analysis

Structural similarity (SSIM) index is a reliable tool to estimate the degree of degradation in images with respect to a reference image [2]. The SSIM is calculated between the image obtained by direct imaging with full aperture and image reconstructions of SMART. The SSIM is given by

$$SSIM(I_1,I_2)=\frac{\left(2\mu_{I_1}\mu_{I_2}+C_1\right)\left(2\sigma_{I_1I_2}+C_2\right)}{\left(\mu_{I_1}^2+\mu_{I_2}^2+C_1\right)\left(\sigma_{I_1}^2+\sigma_{I_2}^2+C_2\right)} \tag{1}$$

where, I_1 and I_2 are the two compared images; μ_{I_1}, μ_{I_2} are the local mean values of the images I_1 and I_2; σ_{I_1}, σ_{I_2} are the variances of the images I_1 and I_2 with the mean values μ_{I_1}, μ_{I_2} respectively; $\sigma_{I_1I_2}$ is the covariance; C_1 and C_2 are constants used to avoid instability when the sum of squares of local mean or variance approaches zero in the denominator. The SSIM index maps and a plot SSIM mean for SMART and direct imaging, are shown in Fig. S2 for *r*=0.2, 0.28, 0.4 and 0.8 *mm*. The brightness in the images indicates the magnitude of the local SSIM index which shows the superiority of SMART over direct imaging clearly.

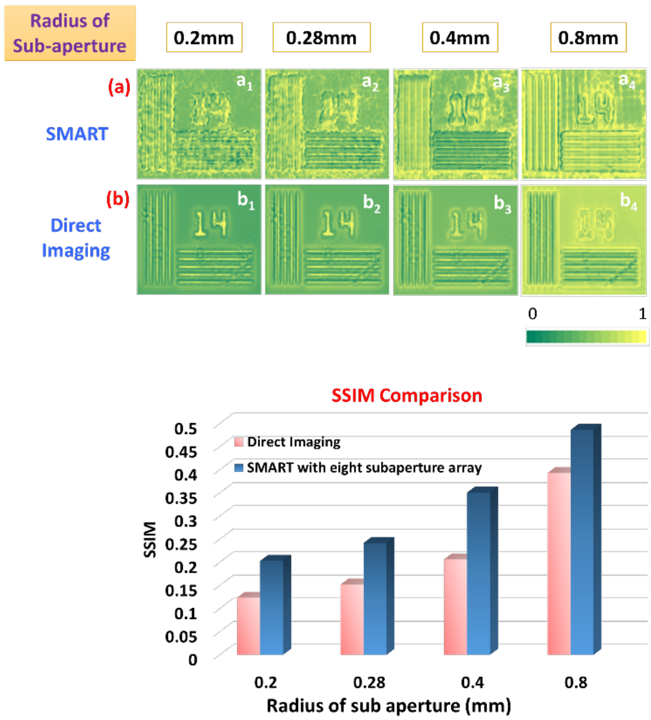

Fig. S2. Top: (a) SSIM index maps of SMART and (b) direct imaging results for *r*=0.2, 0.28, 0.4 and 0.8 *mm* with full aperture direct imaging as reference image. Bottom: Plot of SSIM mean versus radius of sub-apertures for SMART and direct imaging.

Visibility curve is plotted in Fig. S3 when four different radii are used for different cases of SMART with twenty-eight permutations, PAIS and direct imaging with sub-apertures at eight equally spaced marginal points. Visibility is calculated by use of the relation $(I_{max}-I_{min})/(I_{max}+I_{min})$. From the Fig. S3 superiority of SMART and PAIS with respect to direct imaging can be understood.

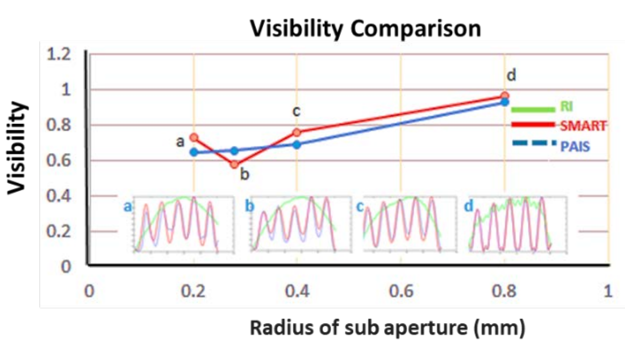

Fig. S3. Plot of averaged visibility of the horizontal and vertical gratings. The plot of the averaged grating is shown as insets for direct imaging, PAIS, and SMART for *r*=0.2, 0.28, 0.4 and 0.8 *mm*.

3. Imaging Objects with a Larger Field of View

The experiments of SMART, PAIS and direct imaging were carried out with two NBS targets namely 14 *lp/mm* and 16 *lp/mm* mounted in the two optical channels and positioned in the same axial location. The two channels were spatially separated in the image sensor to avoid interference between the two optical fields. The reconstruction results of PAIS, direct imaging and SMART are compared when the two objects are located in the same axial position. The results are given in Fig. S4 with four columns corresponding to radii *r*=0.2, 0.28, 0.4 and 0.8 *mm*, respectively. In Figs. S4(a) and S4(b), the reconstruction results of PAIS and direct imaging results with a pair of sub-apertures are shown respectively. Similar comparisons of PAIS and direct imaging with 8 sub-apertures are shown in Figs. S4(c) and S4(d), respectively. Figs. S4(e) shows the reconstruction results of SMART with a pair of sub-apertures in all possible permutations of 8 positions. Note that the reconstruction results of Fig. S4 are similar to that of the single plane experiment with 14 *lp/mm*, shown in Fig. 6 of the main article. In both cases, SMART can reconstruct images of objects with small details that cannot be resolved by the direct imaging or by PAIS. Comparing Figs. 6 and S4, one can see that the reconstruction results of the wide field-of-view (FOV) object (14 *lp/mm* and 16 *lp/mm* in Fig. S4) are worse than smaller FOV object (only 14 *lp/mm* in Fig. 6). By comparing Figs. S4(e_1-e_4), one can see that when the radius of the sub-aperture is decreased from *r*=0.8 to 0.2 *mm*, the resolution of the 16 *lp/mm* target decreases gradually and at *r*=0.2 *mm* the grating lines are no longer resolved. However, the strips of the stay-alone target of 14 *lp/mm* can be resolved in Fig. 6. The reconstruction results of SMART are still better than that of direct imaging even when the field of view was doubled.

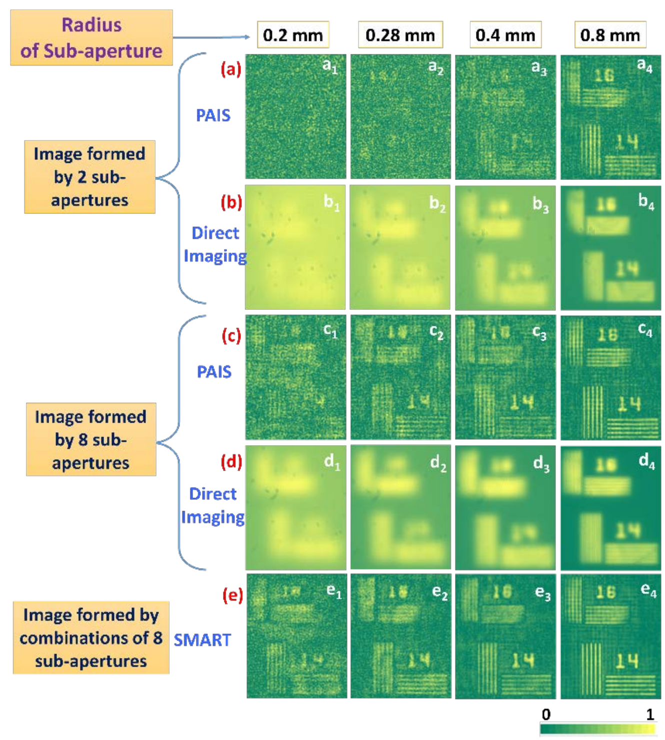

Fig. S4: (a) Reconstruction results of PAIS with 2 sub-apertures, (b) direct imaging results through 2 sub-apertures with a diffractive lens, (c) reconstruction results of PAIS with 8 sub-apertures, (d) direct imaging results through 8 sub-apertures with a diffractive lens, (e) reconstruction results of SMART. All results are given for sub-aperture radii of *r*=0.2, 0.28, 0.4 and 0.8 *mm*.

4. Experiment with two SLMs

To verify the feasibility of SMART to work with two sub-apertures positioned at two different SLMs, a laboratory setup was built using two SLMs separated by a distance such that each SLM acts as a sub-aperture. This configuration is in contrary to the previous arrangements in which all the sub-apertures were displayed within a single SLM. This optical configuration resembles the envisioned satellite telescope model more closely than the previous case of a single SLM. In the laboratory experiment of two

SLMs acting as the two sub-apertures, PAIS is compared against direct imaging.

The optical configuration of the PAIS setup with two separated SLMs is shown in Fig. S5. In this setup, two pinholes are mounted in the two optical channels at the same axial distance and are illuminated using two He-Ne (λ=632.8 *nm*) lasers. The two-point objects were located at a distance of 2 *m* from the two SLMs (Holoeye PLUTO, 1920×1080 pixels, 8 μm pixel pitch, phase-only modulation). The two SLMs were separated by a distance of 2 *cm* (center-to-center) and an area of 8 *mm* in each SLM was used for displaying the phase masks for direct imaging and PAIS. The light from the two-point objects was combined using a beam splitter and is incident on the two SLMs after being deviated by two mirrors M_1 and M_2. A polarizer was used to polarize the light along the active axis of the SLMs. A diffractive lens with a focal length of 52 *cm* was used for imaging the object on an image sensor (Thorlabs USB 3.0 CMOS, 1936 × 1216, 5.86 μm pixel pitch, Monochrome) located at a distance of 70 *cm* from the two SLMs. Since the light from the two SLMs are focused on the same point on the image sensor, an interference pattern is generated across the image since the setup behaves as Young's double-slit experiment [3].

The two point objects were mounted in the two optical channels at the same axial distance but with some lateral separation, and they are imaged using both direct imaging as well as PAIS (for a single pair of apertures SMART and PAIS are actually the same). The experimental setup was first simulated in the computer where the optical fields were calculated using scalar diffraction formulation. In the case of PAIS, three pairs of CPMs were synthesized using GSA to generate a uniform magnitude in the spectrum domain with a space constraint of 110×110 pixels out of 1080×1080 pixels. The synthesized CPM pairs were multiplied by the diffractive lens with linear phases to overlap the two light spots from the two SLMs on the image sensor. The images of the single hologram and the amplitude and phase of the complex hologram obtained from three camera shots for a point object are shown in Fig. S6. The simulation and experimental results of PAIS and direct imaging for a point object and two points are shown in Figs. S7(a) and S7(b), respectively. A low pass filter was implemented to remove the fringe pattern from both direct imaging and PAIS. The reconstruction results of PAIS depicted in Figs. S7(b_1) and S7(b_3), shows two resolved spots with suppressed sidelobes, while the direct imaging shown in Figs. S7(b_2) and S7(b_4), is unable to resolve the two spots due to the presence of higher sidelobes. In another experiment, the simulated direct imaging and PAIS reconstruction results, before and after filtering, are shown in Fig. S8. From the simulation and experimental results, the superior imaging capabilities of PAIS are once again evident. These results reconfirm the validity of the conclusion derived from the previous experiments on the superiority of PAIS and SMART. Moreover, these experiments extend the applicability of SMART to more realistic experimental conditions with two independent non-connected sub-apertures.

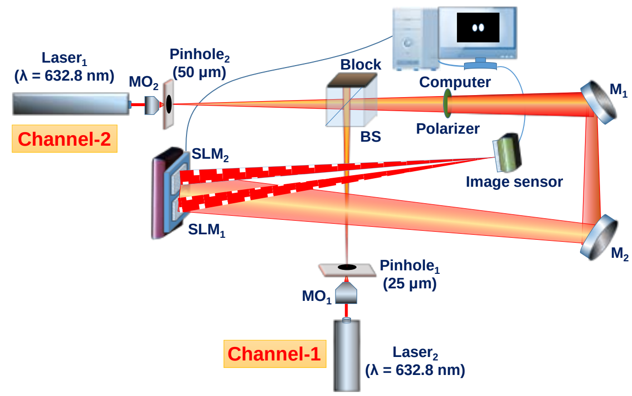

Fig. S5. Optical configuration of PAIS with two SLMs. BS– Beam Splitter; M_1 and M_2 – Planer Mirrors; MO_1 and MO_2 – Microscope Objectives; SLM_1 and SLM_2 – Spatial Light Modulators.

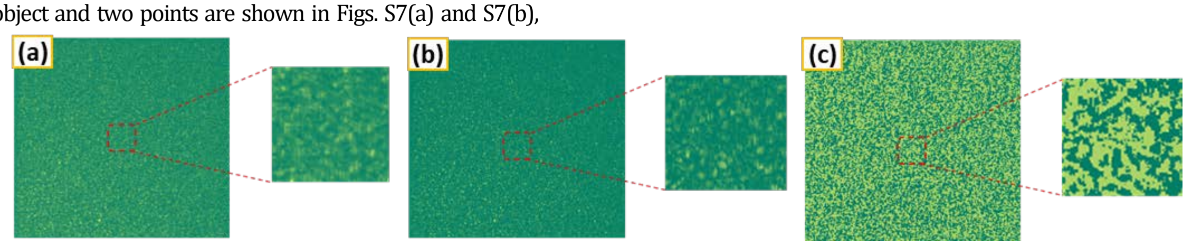

Fig. S6. Images of (a) single camera shot for a point object, (b) amplitude and (c) phase of the complex hologram generated from three camera shots with three different pairs of CPMs.

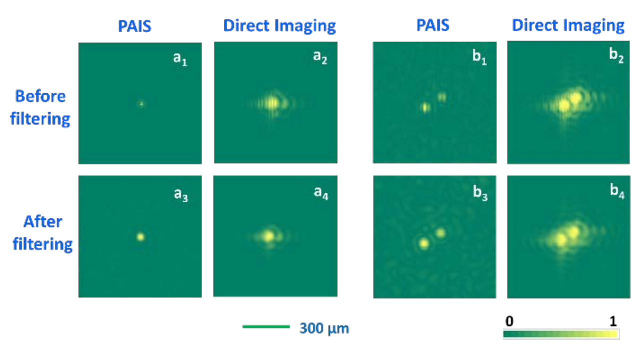

Fig. S7. Experimental results of a single point object, (a_1) PAIS reconstructed image before filtering, and (a_3) after filtering. (a_2) Direct imaging before filtering and (a_4) after filtering. Experimental results for two-point object separated in the diagonal direction, (b_1) PAIS reconstructed image before filtering and (b_3) after filtering. (b_2) direct imaging before filtering and (b_4) after filtering.

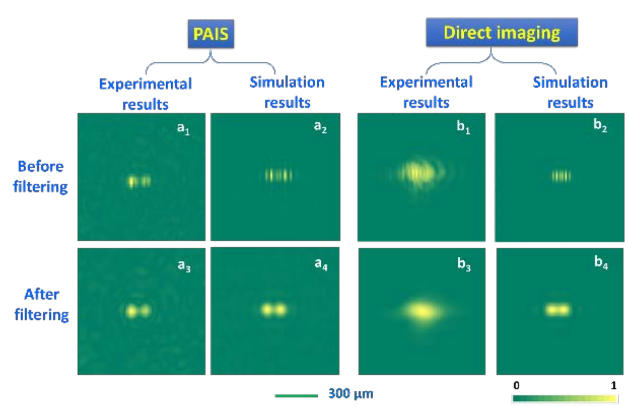

Fig. S8. Reconstruction results of PAIS with a pair of sub-apertures (a_1) before filtering, (a_2) after filtering and simulation results (a_3) before filtering and (a_4) after filtering. Direct imaging results with a pair of sub-apertures (b_1) before filtering, (b_2) after filtering and simulation results (b_3) before filtering and (b_4) after filtering.

References

1. M. R. Rai, A. Vijayakumar, and J. Rosen, “Single camera shot coded interferenceless coded aperture correlation holography,” Opt. Lett. **42**, 3992-3995 (2017).
2. Z. Wang, A. C. Bovik, H. R. Sheikh, and E. P. Simoncelli, “Image quality assessment: From error visibility to structural similarity,” IEEE Trans. Image Process. **13**, 600-612 (2004).
3. B. E. A. Saleh, and M. C. Teich, *Fundamentals of Photonics*, 2nd edn. Ch. 11 (Wiley 2007).